Check for updates

Case History

Field-scale and site-specific permeability of sandstone reservoirs using a stabilized Monte Carlo algorithm: A case study

Uma Vadapalli[1], Ajay Malkoti[1], Nimisha Vedanti[1], V. P. Dimri[1], and Harini Guruhappa[1]

ABSTRACT

The permeability of sandstone varies significantly from site to site at the field scale. Well-established methods for permeability estimation depend on laboratory-measured parameters, which are available only at sparse locations. To overcome such dependency, we have developed a method to estimate sandstone's site-specific and field-scale permeability using well log and interconnected porosity data, respectively. We have considered sandstone as a mono-dispersed porous medium with monofractal pores and simulated them using the fractal theory-based acceptance-rejection Monte Carlo algorithm. Stabilization of the algorithm through an error convergence scheme generated repeatable and reliable permeability values. We tested this developed method on cores from various formations representing clean/shaly sandstones and a few sandstone samples contaminated by carbonates. Compared to laboratory-measured permeability, the estimates are within one-order magnitude error bounds for clean/shaly sandstones and higher for samples that are either contaminated by carbonates or have higher pore volume normalized surface area. We applied the method to infer field-scale permeability trend to explain the unexpected movement of hydrocarbons in the Kalol reservoir lying in the Balol oil field of Cambay Basin India, where the in-situ combustion enhanced oil recovery process is implemented. The field-scale permeability trend could explain the northward movement of the hydrocarbons to the adjacent oil field, Lanwa. It was also observed in the production data of the Lanwa field that the in-situ combustion in Balol has benefited oil production in its wells.

INTRODUCTION

Permeability determines the ease of fluid transmission, which occurs through connected pore spaces in reservoir rocks. In hydrocarbon reservoirs, the fluid-flow pattern, production rate, and the amount of producible hydrocarbon are controlled by the permeability distribution. The permeability of a reservoir depends on several factors, out of which lithology and pore structure are the most crucial. Thus, a permeability prediction method should consider an accurate pore structural and a lithofacies-constrained model. We observe a lateral and vertical transition in lithologies, which result in permeability variation with respect to depth at a specific location in a reservoir and also spatial variations in a field. The field-scale variation in permeability considers spatial variations within a reservoir formation and also the variations occurring in different formations of similar lithology in a field. Therefore, precise information on both is required to generate reliable reservoir models, which can be used for simulations.

The standard practice of measuring a reservoir's permeability is either from pressure drawdown/build-up tests in a well or by laboratory experiments on core samples (Ryou, 1996; Ayan et al., 2001). The former provides only an average over an area and does not capture the field-scale permeability variations. The cores provide site-specific values and also may provide insight into field-scale variability if sufficient measurements are available. The well tests and laboratory measurements are difficult to obtain and provide only sparse information, which is inadequate to generate a reliable field-scale permeability distribution. Alternatively, permeability

estimation methods provide a way to obtain denser information. Frequently used methods to estimate permeability are empirical relations (Bryant et al., 1975; Sen et al., 1990; Luffel et al., 1991; Nelson, 1994; Binley et al., 2005) and empirical models (Katz and Thompson, 1986; Banavar and Johnson, 1987; Pape et al., 1987, 1999; Mavko and Nur, 1997). The empirical relations obtained through regression analysis on available measurements relate permeability to the parameters, namely porosity, pore/grain diameter, specific-surface area, etc. Such relations are controlled by fitting constants and exponents, which are not obtained from lithology or pore structure. On the other hand, the empirical models (Kozeny, 1927; Carman, 1956; Pape et al., 1999) consider pore structure and lithologic variations in terms of pore volume normalized surface area (S_{por}), interconnected pore radius, and the formation factor (F), which are difficult to obtain accurately, thus limiting their field-scale applications. Further studies on using measurements of spectral-induced polarization (SIP) parameters also revealed that field-scale prediction of sandstone's permeability is challenging due to the strong dependence on F, whose value cannot be determined precisely (Weller et al., 2015a; Robinson et al., 2018). Thus, instead of directly considering previously mentioned intractable pore microstructural parameters, the interconnected porosity data are preferred to model the porous medium's realistic structure.

Reliable porosity data can be obtained from well logs or formation evaluation reports or seismic reflection data (Angeleri and Carpi, 1982; Doyen, 1988; Hampson et al., 2001; Vedanti et al., 2015). The controlling factors of porosity are grain shape, size, sorting, and clay filling, which affect the tortuousness of capillaries inside the volume and the diameters of the pores on a cross section (Tiab and Donaldson, 2015). Such tortuous interconnections and pore-diameter distribution at a larger scale are self-similar versions of these parameters at a smaller scale and are fractals (Krohn, 1988; Wheatcraft and Tyler, 1988; Pitchumani and Ramakrishnan, 1999; Dimri, 2000; Yu and James Lee, 2000; Radlinski et al., 2004; Geng et al., 2016, 2018; Liu et al., 2020). Earlier studies used fractal theory for estimating permeability and considered a few parameters such as fractal dimensions, maximum pore diameter, effective capillary diameter, and porosity to represent the structure of the porous medium (Pape et al., 1999; Ramakrishnan and Pitchumani, 2000; Yu and Cheng, 2002; Yu and Liu, 2004). However, in those studies, the simulation of a realistic porous model considering the variations in tortuousness and pore-diameter distribution was lacking. To include this, Yu et al. (2005) propose a stochastic simulation approach based on fractal theory and the Monte Carlo (MC) integration technique for a bidispersed porous medium of sintered copper. Subsequently, several researchers applied the method to estimate the permeability and thermal conductivity of the bidispersed porous media (Zou et al., 2007; Feng et al., 2008; Xiao et al., 2012; Xu et al., 2013). However, it is necessary to have a precise MC algorithm for generating the fractal distribution of sandstone pores for the following reasons:

1) Sandstone acts as a mono-dispersed porous medium in which the contribution of microporosity to permeability is negligible. Thus, the algorithm should be able to ignore micropores and simulate monofractal pore-size distribution in the porosity range of sandstone.
2) The simulation for a realistic sandstone porous model should consider clay contamination and grain-size variations, which

are required to model variations in capillaries' tortuousness and pore diameters.
3) The MC simulation for producing a fractal probability density function (PDF) generates a skewed distribution of samples, in which case the median represents the model estimate instead of the mean.
4) Using conventional MC simulation, the estimated permeability of a porous medium is not repeatable due to large statistical errors caused by dispersion and correlation effects in the simulation.

Thus, to address these issues, we developed a fractal theory-based acceptance-rejection Monte Carlo (FARMC) method. This method uses interconnected porosity data, obtained using bulk density and gamma-ray (GR) logs, and the porosity map of a reservoir formation to predict site-specific and field-scale permeability, respectively, without depending on other laboratory-measured parameters. The application of the method is validated with laboratory-measured permeability of various sandstone core samples from the literature (Zhang and Weller, 2014; Weller et al., 2015a, 2015b, 2016; Robinson et al., 2018) and with the other well-established methods such as PaRiS, Katz and Thompson, and SIP (Katz and Thompson, 1986; Pape et al., 1987; Robinson et al., 2018). The main contributions of the present study are

1) developing an error minimization scheme to attain stability by removing initialization bias and correlation effects in the MC simulation for a repeatable permeability prediction
2) development of the empirical relations predicting microporosity and shale volume from interconnected porosity in sandstone
3) generation of a field-scale permeability map of the Kalol sand reservoir formation in the Balol oil field to understand the fluid movement during the in-situ combustion enhanced oil recovery (EOR) process implemented in the reservoir.

THEORY

Fractal description of a porous model

In a 3D porous volume, grains are cemented by matrix material, and the connected pores between the grains form a bundle of numerous tortuous capillary tubes with uniform diameters appearing as nearly circular pores on a 2D cross section, normal to the flow direction (Figure 1). The tortuous length (L_t) of capillaries and the number of pores appearing on the cross section obey the following two fractal pore laws due to their self-similarity (Pitchumani and Ramakrishnan, 1999):

$$L_t(\lambda) = L_0^{D_t}/\lambda^{D_t-1}, \qquad (1)$$

$$N_{por}(\lambda_0 \geq \lambda) = (\lambda_{max}/\lambda)^{D_p}. \qquad (2)$$

Here, $1 < (D_p, D_t) < 2$, D_t is the fractal dimension for tortuosity (along the flow direction), D_p is the fractal dimension of pores, L_0 is the characteristic length of a capillary, and λ_{max} is the largest possible pore-diameter. In equation 1, pores with a smaller diameter (λ) result in more tortuous and longer capillaries and vice versa (Figure 1). The cumulative number of capillaries/pores (N_{por}) with

representative diameter λ_0, is inversely proportional to the scale λ raised to D_p. Its value reaches the maximum possible number of pores $N_{\mathrm{por,max}}$ for a minimum diameter ($\lambda_{\min}$); thus,

$$N_{\mathrm{por,max}}(\lambda_0 \geq \lambda_{\min}) = (\lambda_{\max}/\lambda_{\min})^{D_p}. \qquad (3)$$

A necessary condition to verify the fractal nature of a porous medium is (Yu and Li, 2001)

$$\left(\frac{\lambda_{\min}}{\lambda_{\max}}\right)^{D_p} \cong 0. \qquad (4)$$

The minimum to maximum pore-diameter ratio ($\lambda_r = \lambda_{\min}/\lambda_{\max}$) plays a vital role in determining the fractal nature of a porous model. The previously described porous model and the fractal power-law relationships also are applicable to sandstone (Krohn, 1988; Wheatcraft and Tyler, 1988; Radlinski et al., 2004).

Fractal nature of sandstone's pore-size distribution

In sandstone reservoirs, pores can be as large as macrosize for clean sand conditions and as small as microsize in the presence of clay (Kuila and Prasad, 2013) (see Appendix A). A unique self-similar pattern is unlikely over such a broad range. Micropores introduce heterogeneity, localized self-similarity in pore-size distribution, and nonlinearity on $\ln(N_{\mathrm{por}})$ and $\ln(\lambda)$ plot (Chen et al., 2017; Lai et al., 2018), indicating a multifractal behavior. The multifractal theory is essential to improve permeability (K) prediction in low-permeability ($K < 1$ mD) tight-sandstone reservoirs (e.g., Ge et al., 2015; Chen et al., 2017; Jiang et al., 2018; Lai et al., 2018). In the case of high-permeability ($K > 1$ mD) sandstone, laboratory experiments on thin sections revealed that sandstone pore-diameters are statistically self-similar over a specific range [$\lambda_{\min}, \lambda_{\max}$] (Katz and Thompson, 1985; Krohn, 1988; Radlinski et al., 2004). Furthermore, within this range, the plot between $\ln(N_{\mathrm{por}})$ and $\ln(\lambda)$ is monotonically linear, which implies that the sandstone can be considered as monofractal excluding micropores ($\lambda < \lambda_{\min}$). Apart from that, in high-permeability sandstone reservoirs, dominant percolation is only through meso to macrosize intergranular pores (Loucks, 2005; Jiang et al., 2018). Thus, the present method ignores the contribution of micropores to permeability and considers sandstone as a mono-dispersed medium (Vadapalli et al., 2014). Thus, in this study, we consider sandstone as a mono-dispersed medium, in which only the wider intergranular porosity (ϕ_u) (see Appendix B) contribute to permeability.

MC simulation for permeability of mono-dispersed sandstone

The equation for permeability of a fractal-porous medium is given as (Yu et al., 2005)

$$k_j = GA^{-(1+D_t)/2} \sum_{i=1}^{N_{\mathrm{por}}} \lambda_i^{3+D_t}, \qquad (5)$$

where λ_i with $i = \{1, 2, \ldots, N_{\mathrm{por}}\}$ is the pore-diameter distribution on a porous cross section simulated using the MC method, k_j is the permeability estimated in one run with $j = \{1, 2, \ldots, N_{\mathrm{run}}\}$, N_{run} is the total number of MC simulations, N_{por} is the cumulative number of pores on the cross section of the porous model, G is the geometric

factor (for a circular capillary tube, $G = \pi/128$), and A is the total area of the squared-porous cross section. We modified the pore structural parameters, A, λ_i, and D_p, for the mono-dispersed sandstone model (see Appendix C), in which useful porosity (ϕ_u) (for definition and estimation, see Appendices A and B) determines the permeability. For a set of λ_i simulated each time, there will be a representative tortuousness of capillaries and cross-sectional area (A_{sim}), as they change with λ (Figure 1). Thus, in each simulation, we assumed that the porous medium has a representative tortuosity ($T = 0.67/\phi_u$ for sandstone; Mavko et al., 2009), the average diameter (λ_{av}), and D_t (modified after Yu, 2005; Yu et al., 2005) for mono-dispersed sandstone. These quantities are represented as follows:

$$\lambda_{\mathrm{av}} = D_p \frac{\min(\lambda_i)}{D_p - 1} \left[1 - \left(\frac{\min(\lambda_i)}{\max(\lambda_i)}\right)^{D_p - 1} \right], \qquad (6)$$

$$A_{\mathrm{sim}} = \frac{1}{\phi_u} \sum_{i=1}^{N_{\mathrm{por}}} \frac{\pi \lambda_i^2}{4}, \qquad (7)$$

$$D_t = 1 + \frac{\ln(T)}{\ln(L_0/\lambda_{\mathrm{av}})}, \qquad (8)$$

where $i \in \{1, 2, 3, \ldots, N_{\mathrm{por}}\}$, λ_{av} is average pore-diameter, A_{sim} is simulated cross-section area, and D_t is tortuosity fractal dimension. The simulation targets to produce the fractal distribution of pores (expressed using equations 2 and 4), whose PDF, $f(\lambda)$ (Yu et al., 2005) and cumulative probability $R(\lambda)$ in the range of $\lambda_{\min}$ to λ are, respectively,

$$f(\lambda) = D_p \lambda_{\min}^{D_p} \lambda^{-(D_p+1)}, \qquad (9)$$

$$R(\lambda) = \int_{\lambda_{\min}}^{\lambda} f(\lambda)d\lambda = 1 - \left(\frac{\lambda_{\min}}{\lambda}\right)^{D_p}. \qquad (10)$$
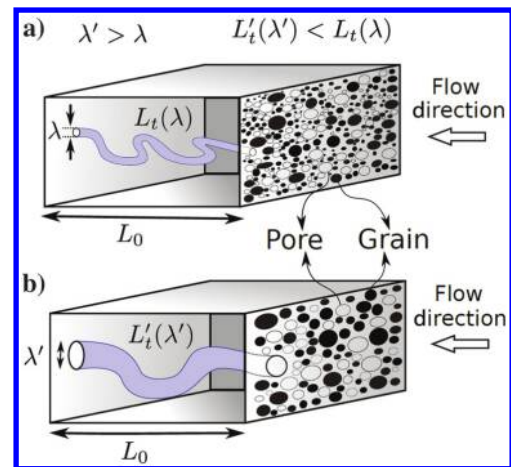

Figure 1. A cross section of porous medium with grains, matrix, pores, and a pore extending as a tortuous capillary tube into 3D volume. (a) A narrower, longer, and more tortuous capillary. (b) A wider, shorter, and less tortuous capillary.

The λ_i obtained from equation 10 and modified for mono-dispersed sandstone using the equations for $\lambda_{\max}$ and λ_r (equations C-1 and C-2) is

$$\lambda_i = \frac{d_{\text{clay}} \sqrt{2(1 - \phi_{\text{u}})}}{d_{\text{eff}}} \frac{\lambda_{\max}}{(1 - R_i)^{(1/D_p)}}, \tag{11}$$

where d_{clay} is the clay diameter and d_{eff} is the effective grain diameter of shaly sand (equation C-6). In equation 10, $R(\lambda_{\min}) = 0$ as none of the pores are taken into account, whereas $R(\lambda_{\max}) = 1$ as all pores are considered. Because λ occurs in the range of $[\lambda_{\min}, \lambda_{\max}]$, the simulation is initiated with a uniform random distribution (R_i), whose probability is $[0, 1]$. Therefore, the λ_i obtained from equation 11 represents the uniform random distribution. However, a fractal distribution is desired. To achieve this, we proposed the FARMC method.

FARMC method

All possible values of λ_i belong to an envelop PDF $g(\lambda)$, which is a uniform distribution:

$$g(\lambda) = \begin{cases} \frac{1}{\lambda_{\max} - \lambda_{\min}}, & \text{if } \lambda_{\min} \leq \lambda_i \leq \lambda_{\max} \\ 0, & \text{otherwise} \end{cases}. \tag{12}$$

The λ_i is accepted if it falls in the target PDF $f(\lambda)$, lying inside $g(\lambda)$ as shown in Figure 2.

In the acceptance-rejection MC method, $g(\lambda)$ and $f(\lambda)$ should satisfy the criteria $0 \leq f(\lambda)/(cg(\lambda)) \leq 1$ (Sigman, 2007). The success probability to obtain λ_i within the target PDF is $1/c$, where c represents the number of iterations required. To understand the implications of c within $[\lambda_{\min}, \lambda_{\max}]$, we analyzed the following two limiting cases.

Case I: $\lambda \to \lambda_{\min}$,

$$c \geq D_p \left(\frac{\lambda_{\max}}{\lambda_{\min}} - 1 \right). \tag{13}$$

This case implies that $c \gg 1$, which requires that $g(\lambda)$ be c times larger than $f(\lambda)$. In addition, $\lambda = \lambda_{\min}$ results in a porous cross section occupied by the maximum number of pores ($N_{\text{por,max}}$) with the smallest possible diameters, which may not contribute to the permeability. Thus, this situation is a limiting case in reservoir sandstones of moderate to good permeability.

Case II: $\lambda \to \lambda_{\max}$,

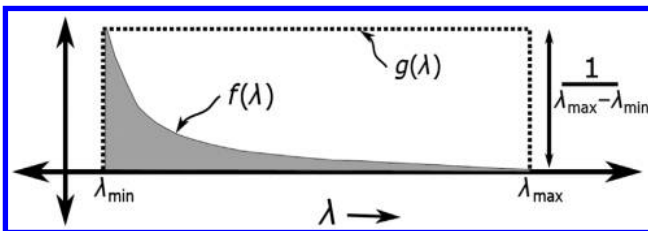$$c \geq D_p \lambda_r^{D_p} (1 - \lambda_r). \tag{14}$$

Figure 2. The uniform distribution and power-law distribution (Yackinous, 2015) representing envelope and target, respectively.

Because $\lambda_r \ll 1$ and D_p lies between one and two, this case results in $c \geq 0$, which requires smaller $g(\lambda)$ to obtain larger success probability. Furthermore, $\lambda = \lambda_{\max}$ results in a porous cross section with a single pore (equation 2). This situation is obviously unrealistic as the porous medium contains numerous pores of variable diameter and c should not be equal to zero. Thus, $\lambda \to \lambda_{\max}$ is a limiting case.

Acceptance criteria

Apart from the formerly mentioned cutoff limits of λ_i, additional acceptance criteria are required to simulate $f(\lambda)$. The constraints only on the range of λ and A_{sim} considered in the previous algorithms (Yu et al., 2005; Zou et al., 2007; Feng et al., 2008; Xiao et al., 2012; Xu et al., 2013) are not sufficient to restrict the total number of simulated pores less than or equal to $N_{\text{por,max}}$ and to obtain the monofractal distribution of pores under the mono-dispersed assumption, over a range of 10%–35% porosity in a sandstone reservoir. Thus, we proposed additional constraints on λ_r and N_{por} for the case of mono-dispersed and monofractal sandstone to satisfy equations 3 and 4. Hence, in total, the MC simulation required four fractal theory-based acceptance criteria:

$$\text{Criterion I:} \quad 0 < R_i < 1 - (\lambda_r)^{D_p}, \tag{15}$$

$$\text{Criterion II:} \quad \lambda_r \leq 10^{-2}, \tag{16}$$

$$\text{Criterion III:} \quad A_{\text{sim}} \geq A, \tag{17}$$

$$\text{Criteron IV:} \quad N_{\text{por}} \leq N_{\text{por,max}}. \tag{18}$$

The first criterion is due to $\lambda_{\min} < \lambda_i < \lambda_{\max}$; alternatively, we imposed bounds on the R_i using equation 11 to constrain R_i as an interior part of the envelope PDF. The second criterion arises due to the dependence of λ_r, D_p, and $N_{\text{por,max}}$ on ϕ_u and d_{eff} to satisfy equation 4 and to maintain the linear monofractal regime on $\ln(N_{\text{por}})$ versus $\ln(\lambda_i)$ in each simulation over a range of 10%–35% useful porosity of sandstone. The third criterion is due to the assumption of the circular pore circumferences, which should encompass the actual pores of irregular circumferences less than or equal to that of the circular pore. The fourth criterion is to maintain N_{por} less than or equal to $N_{\text{por,max}}$ (equation 3) so that the simulation does not produce too many minute pores ($\approx \lambda_{\min}$) to occupy the cross-sectional area and to honor criterion III.

Stabilizing dynamic FARMC simulation

The limiting cases $\lambda \to \lambda_{\min}$ and $\lambda \to \lambda_{\max}$ require a larger $g(\lambda)$ at one end and a smaller $g(\lambda)$ at the other end, respectively, because the pore-size distribution is fractal, which is a power-law PDF. As seen in Figure 2, toward $\lambda_{\max}$, the success probability ($1/c$) of the target power-law PDF decreases, and due to the uniform nature of the chosen $g(\lambda)$, a larger area has to be rejected. As a consequence, the FARMC simulation enters a dynamic state, in which the simulation produces different results in repeated computations, for the same inputs unless N_{run} is sufficiently large. This nonrepeatability is due to the "initialization bias" in the initial transient phase and au-

tocorrelation effects (Sokal, 1997; Janke, 2002, 2008). The initial transient phase is a nonequilibrium state, does not represent a stable target PDF, and leads to instability. A significant dispersion persisting in this phase introduces a systematic error (bias) to the mean unless sufficient numbers of simulations are performed. The autocorrelation effect can introduce additional error to the mean and its effect can be measured in terms of an integrated autocorrelation time (τ_{int}). Although for small standard error (Δ_s) this effect is negligible (see Appendix D). The initialization bias can be removed either by ignoring the samples simulated before the exponential autocorrelation time (which is difficult to predict), or by ignoring the initial $N_{run}/5$ number of samples (Sokal, 1997). Nevertheless, it is possible that this will mistakenly remove the samples in the equilibrium state. Therefore, we propose the following process for a stable MC simulation that avoids the initial transient phase and the autocorrelation effect (by obtaining a reasonably small Δ_s):

1) Increase N_{run} in multiples of two until Δ_s is less than the proposed permissible error limit, $\Delta_{s,max}$ (i.e., $\Delta_s < \Delta_{s,max}$) and the last three consecutive bin series have descending Δ_s values to indicate convergence. Consider the final N_{run} as the reference for the number of iterations required to simulate uncorrelated samples.
2) Ignore the samples before the commencement of convergence in Δ_s for removing initialization bias.

The implementation sequence for acceptance and stabilization criteria on the well-log and porosity data to obtain site-specific and field-scale permeability is given in the FARMC algorithm (see supplemental Table S1).

APPLICATION OF THE METHOD

The FARMC method is first verified on field-scale core data gathered from the literature (Zhang and Weller, 2014; Weller et al., 2015a, 2015b, 2016; Robinson et al., 2018). The data consisted of measured porosity (ϕ_m), measured permeability (K_m) for 107 samples, and measured S_{por} for 79 samples (see supplemental Table S2). The core samples belong to various sandstone formations from different geologic conditions. A detailed description of these core samples and physical property measurements is available in Zhang and Weller (2014), Abuseda et al. (2016), and Robinson et al. (2018). A brief description of the lithology of the formations is given in supplemental Table S2. After verification, the method is applied to the field-scale porosity map and the site-specific porosity of the Kalol reservoir in the Balol heavy oil field situated in Cambay Basin, India.

The study area: Balol heavy oil field, Cambay Basin, India

In the northern Cambay Basin, the Balol field, shown in Figure 3, is situated in the northwest–southeast-trending Santhal-Balol-Lanwa heavy oil belt, in which the fields have strong aquifer support to the east. In this belt, the Kalol Sand (KS) is a reservoir formation pinching-out to-

wards the northwest and reaching a maximum thickness towards the east. This formation extended in most of the northern Cambay fields is comprised of 12 stacked pays, which are grouped into three members — Sertha, Kansari, and Wavel (Bhandari and Chowdhary, 1975; Figure 3). The Wavel member hosts the pay sands, Upper Suraj Pay (USP), KS-I, KS-II, and KS-III. In the Balol field, heavy oil reserves are in KS-I and KS-II, which are unconsolidated, coarse to fine-grained, and contaminated with dark-brown shale along with thin streaks of coal and hard carbonaceous sandstone (Bhandari and Chowdhary, 1975). The porosity and permeability of the Kalol reservoir units in this belt range between 20%–36% and 3000–8000 mD, respectively, and the KS-I pay spread in the three fields has better reservoir characteristics than KS-II (Chowdhary, 2004; Kumar and Mohan, 2004; Kumar et al., 2006). The Kalol reservoir hosts heavy-oil reserves in a northward trap formed with the support of a north–south-trending regional fault (Chowdhary, 2004). Due to the heavier nature of oil, primary recovery was only 10%–12% (Adabala et al., 2007). Thus, in-situ combustion, a thermal EOR process was initiated by putting-on ignition into injector wells. It was observed that, shortly after the ignition, two wells from the neighboring field Lanwa indicated unexpected increased production (Kumar et al., 2008; Zadeh et al., 2010; Vedanti et al., 2015).

RESULTS

Stability of the algorithm

The MC simulation may not produce stable or repeatable results if it is in a "dynamic state" due to insufficient N_{run} or larger $\Delta_{s,max}$. In Figure 4, the initial-transient-dynamic-state is obvious from the fluctuations in Δ_s and the sample mean of k_j, during the initial runs. After performing sufficient N_{run} simulations, the Δ_s declines toward $\Delta_{s,max}$ indicating convergence, and the sample mean also stops fluc-
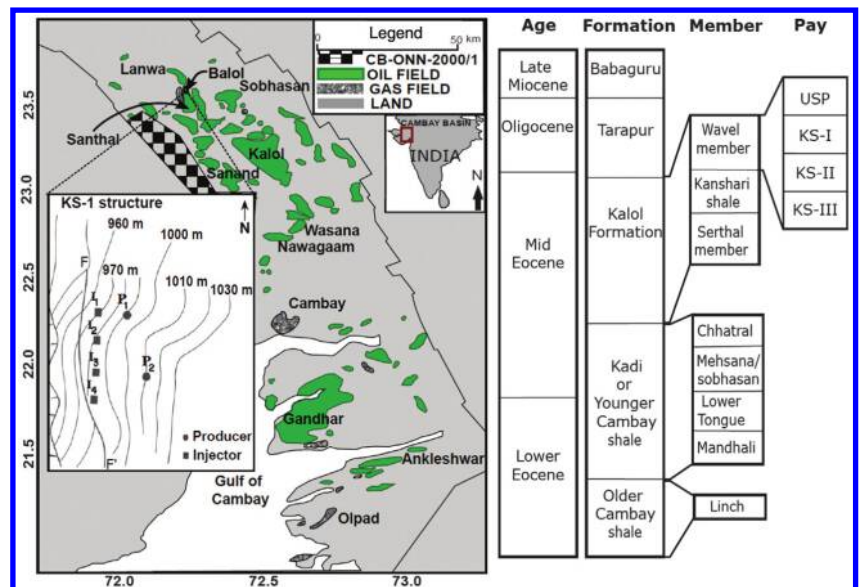

Figure 3. Oil and gas fields in the Cambay Basin, India. Major fields are labeled with names. The location of the Balol field is identified. In the inset figure, the solid lines represent the depth contours at the top of the Kalol reservoir in the northern Balol field, FF′ is the north–south-trending fault, I_1 to I_4 are injector wells, and P_1 and P_2 are production wells (Vedanti and Sen, 2009). The stratigraphy in the Balol field is shown on the right in a tabular form.

tuating, indicating stabilization occurring at suitable $\Delta_{s,\max}$. Table 1 summarizes that a larger $\Delta_{s,\max}$ ensured convergence at a smaller N_{run}; however, the estimated K in the two computations differed significantly because the simulation in the initial transient phase produced biased results each time. With decreased $\Delta_{s,\max}$, the N_{run} increased, which led to the stabilized simulation. Thus, in repeated computations, the difference in estimated K is reduced and becomes negligible for $\Delta_{s,\max} = 5$, indicating a suitable error limit in the range of 24%–35% of ϕ_u. A stabilized simulation produces similar values of K in repeated computations of the algorithm applied to a given porous cross section.

Observance of fractal nature

To confirm the fractal nature of the simulated porous model, the pore-size distribution (λ_i) is presented as a plot between $\ln(\lambda)$ and $\ln(N_{\text{por}})$. Such a plot is shown in Figure 5a for a clean sand ($\phi_u = 35\%$) and a shaly sand ($\phi_u = 16\%$) zone belonging to the Kalol reservoir zone in the well P_1. If $\lambda_r \leq 0.01$, the pore-size distribution showed monotonically linear behavior, and the negative slope of the linear plot is approximately equal to the D_p estimated using equation C-3, indicating monofractal behavior in the clean sand and the shaly sand. If λ_i is multifractal, the slope will deviate significantly from the value of D_p (equation C-3) due to the staircase effect. With the increased values of λ_r (≥ 0.01) in the simulation of shaly sand, we can see that a portion of the plot is showing a linear regime and another is showing a staircase effect indicating the coexistence of monofractality and multifractality. At a much larger λ_r, the dominant staircase effect indicates multifractal pores. In general, multifractality arises due to the lack of a simple self-repeating pattern over a broad range (Xue and Bogdan, 2017). In porous geologic media, evidenced multifractal behavior (Figure 5a) may indicate a change in the pore-scale regime due to lithologic inhomogeneity leading to a broader range of pore diameters. The histogram of permeability samples

(k_j) corresponding to each lithologic block is shown in Figure 5b, which resembles the power-law PDF. The histogram transformed toward the symmetric distribution deviating from a pore law, with reduced ϕ_u or increased shaliness. This could be due to ignoring micropores in the formulation of acceptance criteria mainly for sandstones and shaly sands. Since k_j follows a skewed distribution, its central value, the median (second quartile, K_{Q_2}), represents the estimated permeability (K) of a reservoir block with distinct ϕ_u. The lower and upper bounds of K are the first (K_{Q_1}) and third quartiles (K_{Q_3}) of the distribution, respectively.

Sensitivity test

In the FARMC method, K depends on several parameters, out of which the important pore structural parameters are the effective grain size (d_{eff}) of the formation and the maximum pore diameter ($\lambda_{\max}$), which can largely affect permeability. In Figure 6, it is clear that K increases with increased d_{eff} and $\lambda_{\max}$. However, K is equal for small differences in d_{eff}, whereas it is distinct even for a small change in $\lambda_{\max}$, indicating that, in the present mono-dispersed-fractal-sandstone model, K is more sensitive to $\lambda_{\max}$ than d_{eff}. We are able to estimate the pore structural parameters for the mono-dispersed sandstone (see Appendix C). Rather the values of the constant a and minimum particle size (d_{clay}) are set in such a way to satisfy the criteria: maximum value of $\phi_c = \phi_i^{\min}$, the minimum value of $\phi_c = 0$, and $\lambda_r \leq 10^{-2}$ for a given ϕ_i data. The variations in K with respect to these data-dependent constants a and d_{clay} are presented in Table 2 and Figure 7a, considering two acceptable pairs of their values on the Bahariya core samples, which covered a broad range of sandstone porosity. Figure 7a clearly shows that K does not vary beyond $\pm e_1$ with the possible variations in a and d_{clay}.

Field-scale permeability estimates

Verification on core-measured permeability

In each formation, we assumed that the highest porosity sample is clean sand and porosity/permeability reduction is due to clay filling. Thus, the sample with the highest measured porosity (ϕ_m) has the highest sand volume (V_{sst})/lowest shale volume (V_{sh}) (equation
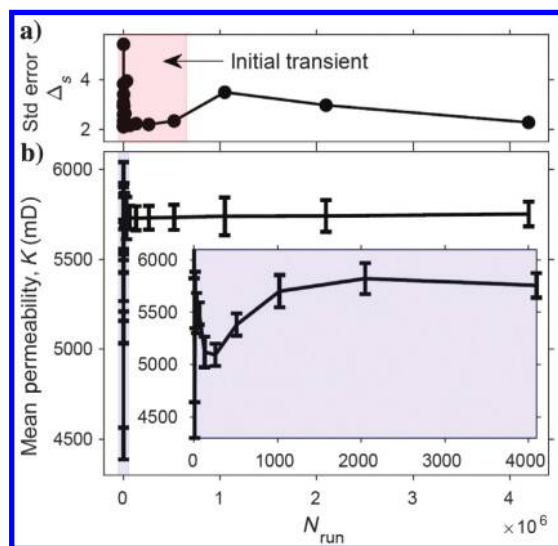

Figure 4. Variations in (a) standard error (Δ_s) and (b) mean permeability, with an increased number of simulations (N_{run}) for $\phi_u = 35\%$. The fluctuations of Δ_s and mean permeability indicate initialization bias. The decline in Δ_s and steadiness in the mean indicate the convergence zone and stabilization, respectively. The error bars of the mean are exaggerated by 30 times for better visualization in (b).

Table 1. The estimated permeability (K) in different computations considering larger and smaller $\Delta_{s,\max}$.

$\phi_u(\%)$	$\Delta_{s,\max}$	Computation 1		Computation 2	
		N_{run}	K (mD)	N_{run}	K (mD)
Well P1					
35	200	2^{10}	4000	2^{11}	4231
35	100	2^{12}	4455	2^{12}	4346
35	50	2^{14}	4317	2^{15}	4367
35	5	2^{22}	4306	2^{22}	4306
GR1					
24	200	2^{12}	504	2^{12}	533
24	100	2^{12}	512	2^{12}	551
24	50	2^{13}	330	2^{13}	400
24	5	2^{18}	377	2^{16}	378

E-2) and highest ϕ_u (equation E-3). The d_{eff}, K, K_{Q_1}, and K_{Q_3} gradually decrease with a reduction in ϕ_m or increased V_{sh} (see supplemental Table S2). The samples with negligible K_m indicate their dominant shale content and fail to meet the acceptance criteria (equation 16); thus, we assigned $K = 0$ (see the supplemental Table S2) using our FARMC algorithm (FARMCA). To demonstrate the reliability of predicted permeability values, a log-log plot between K_m versus K is shown in Figure 7b. The K values within the one-order magnitude error bounds ($\pm e_1$) are reliable predictions (Figure 7b). We observe in the supplemental Table S2 and Figure 7b that the permeability of LRF, SPF, a few of SS (C3-CI-139.7, C3-P-021, and C3-P-023), and Shahejie (CS-1) are beyond $+e_1$, indicating significant uncertainty in prediction. These samples have either high $S_{por}(\geq 60)$ or are suspected to contain carbonates (dolomite or calcite) and have extremely low permeability despite having good porosity. We computed the absolute logarithmic mean deviation $\varepsilon = (1/N_{sam})\Sigma_{i=1}^{N_{sam}}|\log(K) - \log(K_m)|$ (N_{sam} is the number of samples) and compared it with other well-established methods in Table 3 to demonstrate that the present method produced $\varepsilon = 0.724$, which is lower than other methods applicable at the field scale.

Permeability contour map at the top of KS-1 pay sand, Balol oil field

The FARMC simulations are performed for estimating location-wise permeability (K) corresponding to distinct ϕ_i digitized from a contour map (provided by the operator). The location-wise variations in ϕ_i and K are fit to 2D surfaces and linearly interpolated at every $1\ m^2 \times 1\ m^2$ grid. The contour maps of the interpolated ϕ_i and K surfaces are shown in Figure 8. We estimated the field-scale V_{sh} and ϕ_u using empirical relations (equations E-2 and E-3), considering that $a = 0.01$ and $d_{clay} = 0.6\ \mu m$. In Figure 8b, the area of interest covering the production and injection wells is shown in a rectangle. Within this area, the highest permeability zone (approximately 500 mD) lies in the middle, and the higher permeability zone (approximately 250−500 mD) extends to the north, i.e., toward the Lanwa field. The injector (I_1) and producer (P_1) are located in a lower permeability zone (≤ 250 mD), and P_2 is located in the least permeability zone. There are significantly higher permeability zones toward the southern side outside the rectangle.

Site-specific permeability estimates

In the site-specific permeability estimation, we initially estimated ϕ_i, V_{sst}, ϕ_c, and ϕ_u using density and GR logs (for the procedure, see the supplemental Table S3) and then performed FARMC simulations to estimate K for each lithologic

block in the well P_1. The estimated quantities are presented as lithologically constrained blocked logs in Figure 9. In Figure 9, the lowest/highest GR values indicate clean sand/shale lithofacies, which correlate with the litholog and also with the estimated V_{sh} and ϕ_c and the highest/lowest values of V_{sst} and ϕ_u. The K is highest for clean sand, reduces with shale contamination, and is lowest for shale. The shale blocks and some shaly sand blocks with $\phi_u < \phi_{u,sh}$ did not meet the constraint (equation 16); thus, we assumed that $K = 0$. The lower and upper bounds of K are shown by the first and third quartiles (Figure 9), respectively, and it may be observed that the interquartile range increases with ϕ_u indicating a reduction in the success probability, which is the inverse of N_{run}. Higher porosity zones require more N_{run} to obtain convergence due to a larger pore area and more pores. The shaly sand blocks obtained either negligible or significant K, according to variations in the fraction of V_{sst} and pore structural and fractal parameters. The pore structural and fractal parameters used in the simulation of each lithologic block, D_t, d_{eff}, D_p, and λ_r, are estimated considering lithologic constraints implicit in equations 8, C-2, C-3, and C-6. Furthermore, we observed that, in Figure 9, d_{eff} reduces with increased V_{sh} because the former represents the weighted average of sand and shale grain radius (equation C-6). Therefore, d_{eff} for the clean sand block is the largest, and its value of 222 μm falls within the coarse-grain-sand category, which agrees with the KS Formation (Chowdhary, 2004). The D_p explains the pore-size distribution on a porous cross section; however, because it depends on several variables, it is difficult to explain its variation. In the present case, we observed that D_p decreases with an increase in V_{sh}, due to decreased ϕ_u and macropore area. The largest D_p is observed for a clean sand block, which indicates a porous cross section occupied by pores with wider diameters leading to the largest
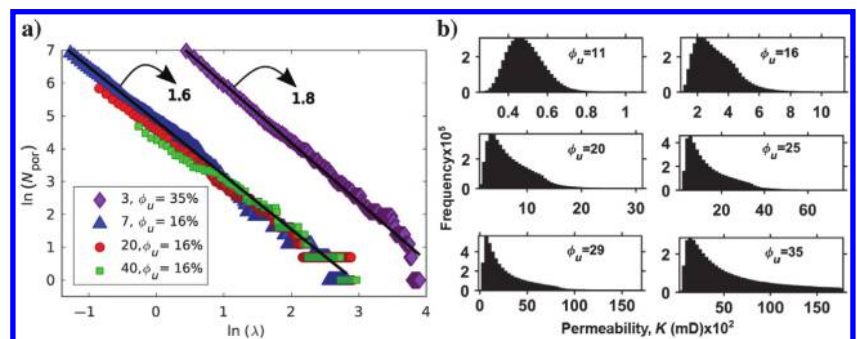

Figure 5. (a) Plot of simulated pores in clean sand block ($\phi_u = 35\%$) (upper) and shaly sand block ($\phi_u = 16\%$) (lower) in the well P_1. The values in the legend indicate $\lambda_r \times 10^{-3}$. The plot is monotonic and linear if $\lambda_r \leq 0.01$ and it shows an increased staircase effect for $\lambda_r > 0.01$. Labels on the plot are negative slopes of the linear least-squares fitted lines, which can be equal to D_p. (b) Histograms of permeability for lithologic blocks with different ϕ_u. The histogram is most/least skewed in the case of the highest/lowest ϕ_u.

Table 2. Estimated permeability (K) for two sets of the data-dependent parameters (a and d_{clay}).

Parameters		Sample name										
d_{clay}	a	B49H	B49V	B4H	B4V	7H1	18H1	22H	28H1	53H2	55	43H1
0.4	0.06	8	8	0	0	50	22	14	115	402	361	492
0.3	0.07	12	12	0	0	49	26	18	96	319	286	389

pore area. The largest D_t can be related to highly tortuous capillaries due to finer particles in shale, whereas in the case of clean sand, the smallest D_t is due to the largest d_{eff} leading to the widest and least convoluted capillaries and the highest K. The λ_r is used to check the acceptance criteria (equation 16) in each block and simulation is not

Table 3. Absolute logarithmic mean deviation (ε) between the measured and the predicted permeability using well-established methods and the present method considering the 57 sandstone samples published in Robinson et al. (2018).

Method	ε
Time constant (τ_{pc} and D_{+spor})	0.539
Time constant (τ_{mean})	0.707
Present method	0.724
Katz and Thompson	0.729
Polarization magnitude (s″)	0.77
Time constant (τ_{pc})	0.779
Polarization magnitude (mn)	0.807
PaRiS model	1.023
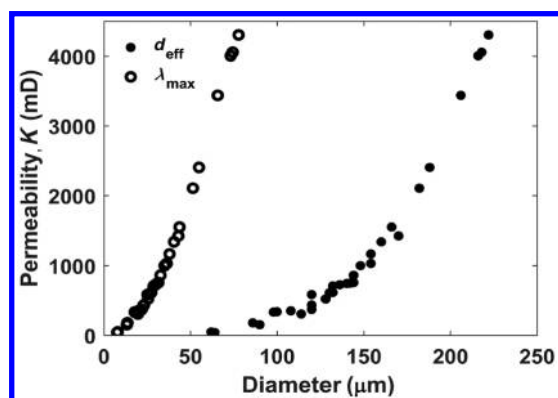
Figure 6. Variations in K with the effective grain diameter (d_{eff}) and maximum pore diameter (λ_{max}) showing its distinct increment with λ_{max}.
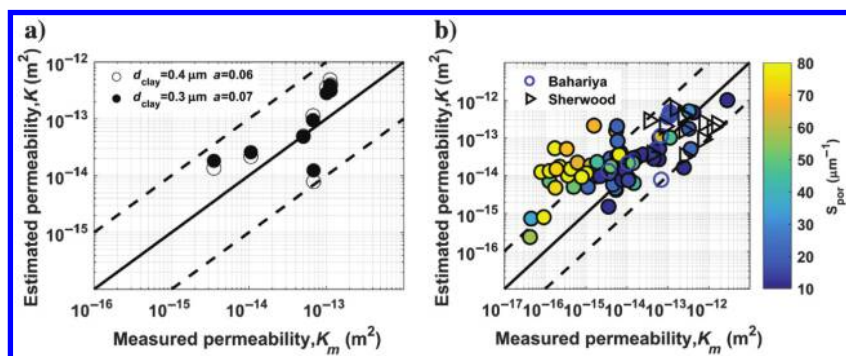

Figure 7. Log-log plot between K_m versus K, (a) considering Bahariya core samples and (b) considering all of the core samples used in the study. The dotted lines show plus or minus one-order magnitude error bounds ($\pm e_1$) about K_m. In (a), values of K estimated using both the pairs of a and d_{clay} are within $\pm e_1$, and in (b), most of the samples with higher (≥ 60) S_{por} lie above $+e_1$.

carried out in the blocks having this ratio greater than or equal to 0.01, which are shown with dotted stems. The blocks with either negligible or significant K act as either baffles or transmission zones for fluid movement.

Lithologic blocks having equal ϕ_i may have different K due to different V_{sh} estimated using the GR log. Such differences in V_{sh} are clear in Figure 10a and 10b (see Appendix E). Figure 10b shows agreement with the well-known Thomas and Stieber model (Thomas and Stieber, 1975; Neasham, 1977; Thomas and Ra, 1977; Mavko et al., 2009). As shown in Figure 10b, point A ($\phi_u = \phi_i = \phi_{i,max}$), line AB, point C, and line CD represent clean sand, sand with increasing laminated shale, sand with clay filling in all interconnected pores, and predominately shale with dispersed quartz grains, respectively. We observe that, with the increase in V_{sh}, ϕ_i linearly decreases (line AB) indicating that laminated shale gradually reduces it, whereas drastically reduced ϕ_u (line AC) indicates the clay filling/dispersed shale blocks intergranular wider pores (see Appendix B). Beyond critical shale content (point C) and even at $V_{sh} = 100$, there is still ϕ_i due to micropores in the shale, which can have interconnected microporosity of approximately 40%–50% when compacted, and as much as 90% when newly deposited as mud (Serra, 1983), with negligible permeability.

DISCUSSION

This study presents an FARMCA, which uses only interconnected porosity (ϕ_i) data (either measured on cores or estimated using a few well logs) to estimate reliable permeability without depending on other laboratory-measured pore structural parameters. The permeability (K) estimated using this algorithm falls within the acceptable error limits ($\pm e_1$) of measured permeability (K_m) for sandstone samples taken from different boreholes in various geologic settings (Figure 7b and the supplemental Table S2), which clearly demonstrates that the algorithm is applicable to site-specific and field-scale permeability estimation problems. Our results agreed with those of Robinson et al. (2018), with the advantage that our method does not need any laboratory-measured parameters like the accurate value of formation factor, as required in the former study. The logarithmic mean deviation ($\varepsilon = 0.724$, see Table 3) of estimated permeability values using this algorithm is lower than the well-established empirical models and polarization-magnitude models, which are preferred at the field scale. The time constant length-scale model (τ_{pc} and $D_{(+spor)}$) with lower ε is however not preferred at the field-scale. The algorithm estimates useful porosity (ϕ_u) to segregate the reservoir zones based on the actual percolating porosity fraction. An advantage of this segregation is that the useful porosity trend represents a qualitative trend of permeability in the reservoir, before spending time on MC simulations or measurements for the quantitative outcome.

In a geologic-porous media, the pore-scale microstructures and lithologic contamination, including diversified mineralogical content, can lead to a complex relationship between porosity and permeability. Because FARMCA uses only porosity data to predict permeability, it finds limitations in two geologic scenarios. The first could be the cracks initiation, as in the case of samples like Elb sandstone (see the supplemental Ta-

ble S2), which is a remnant of long-lasting erosion, and the second case is where permeability is lower than expected due to higher S_{por} (≥ 60, the supplemental Table S2) or sandstone contaminated by carbonates (calcite or dolomite). In the first case of cracks initiation, permeability is underestimated as the present model considers only interconnected pores forming tortuous capillaries, not conduit-like cracks. Secondary porosity such as cracks can deviate the sandstone pores from the monofractal distribution, and that might need a multifractal approach, which is beyond the scope of the present study. In the second case, the model and equation E-2 may not capture the required mineralogical variability. This may lead to underestimation of shale volume (V_{sh}) leading to overestimated K (falling above $+e_1$ in Figure 7b). Robinson et al. (2018) show that well-established SIP models also overestimate permeability (above $+e_1$) for samples with higher S_{por} (≥ 70) or dolomite.

We have shown with the sandstone samples used in the verification of the algorithm (Figure 7b and the supplemental Table S2) that the method is applicable to different geologic conditions. Thus, we applied the algorithm to estimate the site-specific and field-scale permeability of the Kalol sandstone reservoir in the Balol oil field of Cambay Basin, India (Figure 8b). Our results show that the estimated permeability (K) of Kalol is within the acceptable range (3000–8000 mD) of the observed permeability range given for the Kalol Formation in the Balol field (Chowdhary, 2004). The site-specific permeability in Kalol delineated the fluid transmission zones and baffles to vertical movement in the producer P_1. Furthermore, the field-scale permeability map prepared using this method demarcates a higher permeability trend in the study area (Figure 8b). Vedanti et al. (2015) also show a high-permeability trend toward the north and northwest of the injector (I_1), on permeability map generated using dense 3D seismic data available in the area (enclosed by a rectangle in Figure 8b). In the former study, a qualitatively drawn permeability map was used to explain the northward movement of fluids in the reservoir. However, for a realistic reservoir modeling and simulation, a quantitative field-scale permeability was required, which was prepared using the proposed algorithm in this study. As shown in Figure 8b, the map shows a higher permeability trend toward the north of injectors, however, both the producers (P_1 and P_2) (Figure 3) are located in a lower permeability zone. We assert that the high-permeability trend might be governing the northward movement of vaporized hydrocarbons toward an adjacent field, Lanwa, and enhancing the oil production in those wells, as reported by Kumar et al. (2008) and Vedanti et al. (2015). The other factors that could be governing the fluid movement are buoyancy drive due to northward updip and small migration pathways due to the structural discontinuities, as discussed by Kumar et al. (2006), Vedanti and Sen (2009), and Zadeh et al. (2010). The buoyancy drive in a reservoir is generally governed by the structural parameters, which can be mapped using seismic and well data. However, to determine the direction of fluid movement, a field-scale permeability
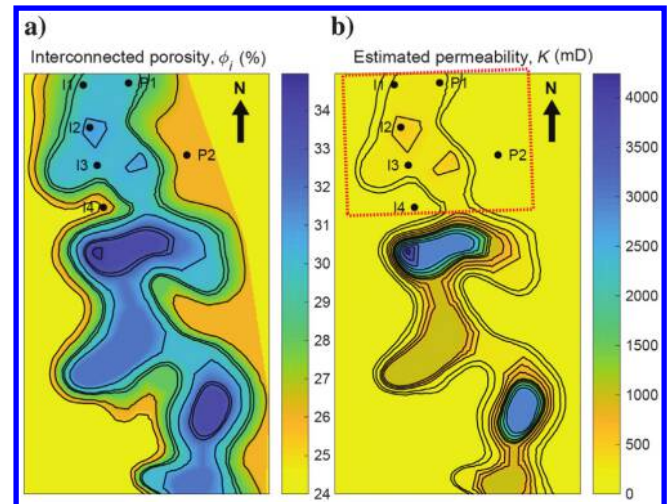

Figure 8. (a) Interconnected porosity (ϕ_i) map and (b) estimated permeability (K) map, on the top of the KS-1 sand pay in Balol oil field, Cambay Basin, India. The area of interest is enclosed by a rectangle. In (b), the higher permeability zone within the rectangle extends toward the north of I_1. Both producers (P_1 and P_2) are in a relatively lower permeability zone compared with I_1, I_2, and I_3. There also are higher permeability zones south of I_4.
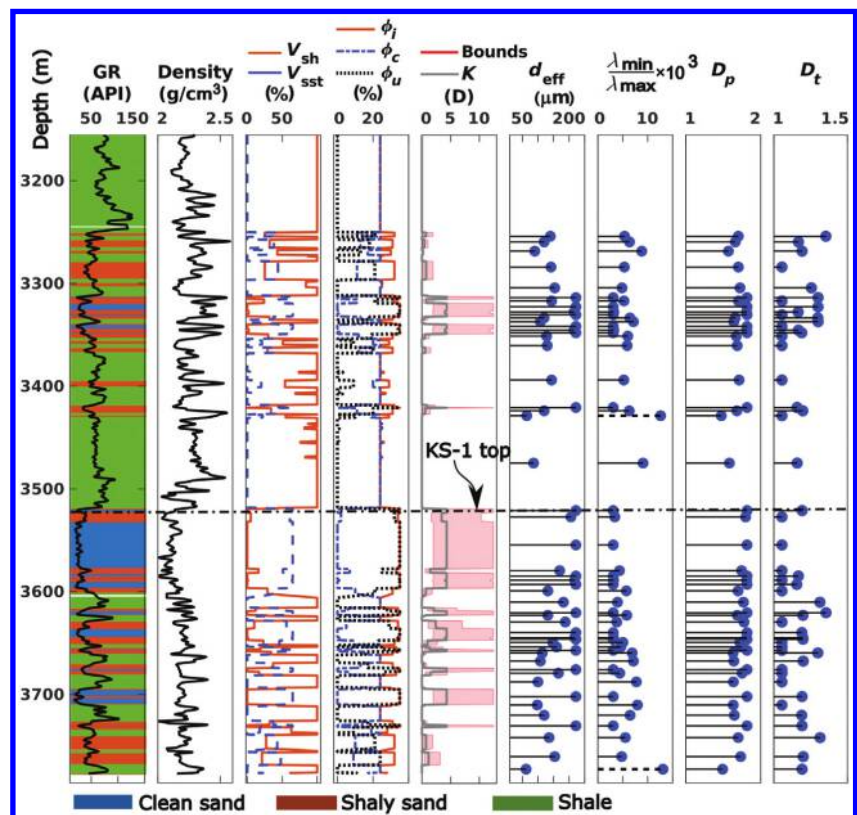

Figure 9. Well logs (density and GR) used in the study and estimated parameters, namely V_{sh}, V_{sst}, ϕ_i, ϕ_c, ϕ_u, and K, in the KS zone in the producer P_1. Interpreted lithofacies are overlapped on the GR log. The shaded area in the plot for K indicates the upper (K_{Q_3}) and lower (K_{Q_1}) bounds. Estimated d_{eff}, D_p, D_t, and λ_r are indicated as a stem for each lithologic block. The dotted horizontal line on the logs indicates the top of the KS-1. The depth for all of the logs is the same as shown in column 1.

trend is required for production planning. A future addition to this study may include a structurally constrained permeability model for sandstone reservoirs by integrating seismic and geophysical well logs.

The field-scale permeability map prepared for the Kalol reservoir would have been more informative if the required porosity map was available in the north of the injector (I_1). Another limitation to this study was nonavailability of geologic structural constraints such as sealing fault and production data in the southern part of the region. Furthermore, we observed discrepancies in site-specific (Figure 9) and field-scale (Figure 8b) permeability values at the producer P_1, which could be due to averaging, while generating interconnected porosity (ϕ_i) maps. In the site-specific case, the in-situ measured GR log is sensitive to minor differences in V_{sh} values, which control the permeability variation in reservoir blocks having the same ϕ_i values, whereas, in the field-scale application, there is no such discrepancy because the empirical relations (equations E-2 and E-3) produced unique V_{sh} and ϕ_u values (Figure 10) for a unique ϕ_i. The calibration of V_{sh} from equation E-2 at multiple wells with GR logs may improve the field-scale shale volume (V_{sh}) estimates and hence the permeability prediction.

In this study, we have shown that the FARMC simulations for a clean sandstone produced a monotonically linear plot (Figure 5a), indicating the monofractal behavior with simple self-similar pores within the linear regime. The advantage of such a monofractal approach is a requirement of only a limited number of fractal parameters (λ_r, D_p, and D_t), which we estimated in the FARMCA without depending on cumbersome measurements. Apart from that, we found that the fractal behavior of pores proposed by Yu et al. (2005) applies only to mono-dispersed and monofractal models in the case of a geologic-porous media because it accepts only $0.32\phi_i$ as the maximum ϕ_c and cannot simulate the shale zones due to their larger ϕ_c. Thus, we modified the existing method of Yu et al. (2005) for a mono-dispersed sandstone. However, the staircase effect in Figure 5a indicates the possible multifractal behavior of shaly sands with $\lambda_r > 0.01$. The multifractal approach is more appropriate for low permeable ($K < 1$ mD) tight sandstone and shale gas reservoirs, where the contribution of micropores is significant (Ge et al., 2015; Chen et al., 2017; Jiang et al., 2018; Lai et al., 2018).

CONCLUSIONS

We developed a method for site-specific and field-scale permeability estimation, considering sandstone as a mono-dispersed and monofractal porous model. This model represents the desired PDF, simulated from the FARMCA overcoming limitations such as initialization bias and correlation effects to produce repeatable permeability estimates. This method predicts the permeability in a way that is insensitive to the variations in data-dependent parameters within the required degree of accuracy for clean/shaly sands. It overestimates permeability for sandstone either contaminated by carbonates or having higher pore volume normalized specific surface area (≥ 60). Thus, the present method provides highly reliable permeability estimates using the interconnected porosity data and does not depend on other laboratory-measured parameters. The present study also demonstrates the crucial role of the gamma-ray log in discriminating different permeability zones having the same interconnected porosity. This observation is vital for site-specific permeability estimation of reservoir zones having different clay content and microporosity.

In a high-permeability ($K > 1$ mD) sandstone, pores can be monofractal within a specified range of diameters, ignoring micropores. Thus, we assumed that the sandstone is monofractal and consists of capillaries with a uniform diameter. To explain the real sandstone scenario, the model used here considers wider less-tortuous capillaries in sandstone and narrower more-tortuous capillaries in shaly sand. Thus, this study provides a method that uses only a few well logs or available porosity information to predict reliable permeability in sandstone reservoirs.

ACKNOWLEDGMENTS

DATA AND MATERIALS AVAILABILITY

Data associated with this research are available and can be obtained by contacting the corresponding author.

APPENDIX A

PORES AND TYPES OF POROSITY

Pores fall into three categories depending on their diameter: macropores, mesopores, and micropores, which have diameters (λ) >50, 2–50, and <2 nm, respectively (Kuila and Prasad, 2013). This appendix also describes the types of porosity considered in this study. Total porosity (ϕ_t) is the fraction of void space available in the total volume of rock. In the case of shaly sand formations, the total porosity includes the sand porosity, which is intergranular porosity, and shale porosity due to connected and nonconnected micropores. Interconnected porosity (ϕ_i) is the porosity contribution of all interconnected pores. Effective porosity (ϕ_e) is the interconnected porosity that allows free movement of fluids, and therefore it excludes nonconnected
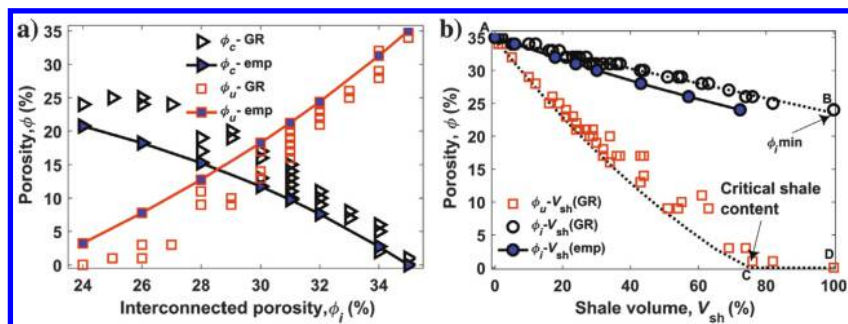

Figure 10. Estimated shale volume (V_{sh}), critical porosity (ϕ_c), and useful porosity (ϕ_u) from empirical relations (equations E-1, E-2, and E-3) (lines with filled symbols), and well logs (dotted lines in [b] are computations from equations B-1 and B-2 and open symbols in [a] and [b] are averaged values for each lithologic block). For a lithologic block of a given ϕ_i, there are multiple values of V_{sh}, ϕ_c, and ϕ_u from the logs, whereas, from empirical relations, these parameters are unique.

porosity, clay-bound water (CBW), and capillary water (CW) in micropores. Critical porosity (ϕ_c) is the fraction of interconnected porosity due to micropores present in the shale and it defines the threshold for percolation. Useful porosity (ϕ_u) is the interconnected porosity devoid of micropores. Because micropores are excluded, the effect of CBW and CW is removed effectively. Therefore, ϕ_u represents the intergranular porosity in excess of the threshold porosity for percolation and determines the permeability. The ϕ_e also determines permeability according to its definition. However, in practice, the ϕ_e estimated using density/neutron/sonic logs or cores in the laboratory does not entirely exclude CBW and CW. Thus, it includes the microporosity and becomes approximately equal to ϕ_i. Therefore, permeability estimation by the present method considers ϕ_u.

APPENDIX B

ESTIMATION OF USEFUL POROSITY

A clean sand transforms to shaly sand by contamination with clay minerals as lamination, filling and replacing or coating on grains and pores to form laminated, dispersed, and structural shale, respectively (Thomas and Stieber, 1975; Neasham, 1977; Thomas and Ra, 1977; Mavko et al., 2009). In consequence, shaly sand consists of wider connected pores in between the sand grains, known as intergranular porosity and also intragranular porosity or microporosity due to dispersed shale (Krohn, 1988). These micropores also can be interconnected. However, because the diameters of micropores are below a threshold, intermolecular attraction prevents fluid circulation. Thus, we subtracted ϕ_c from ϕ_i to obtain the wider fraction of porosity (ϕ_u) that has a major contribution to percolation. The equations proposed in Vadapalli et al. (2014) are used to estimate ϕ_i, ϕ_c, and ϕ_u. Initially, the effects of laminated shale are applied in the corrected bulk density log ($\rho_{b,\text{corr}}$), and then ϕ_i is obtained as follows:

$$\phi_i = \frac{\rho_{b,\text{corr}} - \rho_m}{\rho_f - \rho_m}, \qquad \text{(B-1)}$$

where $\rho_{b,\text{corr}} = \rho_{b,\text{clean}}(1 - V_{\text{sh}}) + \rho_{b,\text{sh}}V_{\text{sh}}$ and $\rho_{b,\text{clean}}$ and $\rho_{b,\text{sh}}$ represent the bulk density for clean sandstone and shale, respectively. The micropores due to dispersed shale are discarded from (ϕ_i) to obtain ϕ_u:

$$\phi_u = \phi_i - \phi_c = \left(\phi_i - \frac{V_{\text{sh}}}{(1 - \phi_i)}\phi_i\right), \qquad \text{(B-2)}$$

where the shale volume $V_{\text{sh}} = 0.083 \times [2^{(3.7I_{\text{GR}})} - 1]$, for tertiary rocks (Larionov, 1969) and $I_{\text{GR}} = [\text{GR} - \text{GR}_{\text{sst}}]/[\text{GR}_{\text{sh}} - \text{GR}_{\text{sst}}]$ where I_{GR} is gamma-ray index, GR represents the gamma-ray reading from the log, and GR_{sst} and GR_{sh} represent the gamma-ray readings to characterize the lithofacies as clean sandstone and shale, respectively.

APPENDIX C

MONO-DISPERSED MODEL OF SANDSTONE

In a mono-dispersed medium, the microintragranular pores formed due to clay dispersion are included in the solid portion. Thus, we replaced the cluster mean radius in a bidispersed fractal-porous model of Yu and Cheng (2002) with an effective diameter (d_{eff}) of sand grain and clay particles, and the minimum particle size with d_{clay} because clay is the smallest particle a sandstone or shaly

sand can be composed of. Thus, for a mono-dispersed sandstone, the theoretical relationships are derived as a function of d_{eff}, d_{clay}, and ϕ_u as follows:

$$\lambda_{\max} = \frac{d_{\text{eff}}}{4}\left[\sqrt{2\left(\frac{1}{1-\phi_u}-1\right)} + \sqrt{\frac{2\pi}{\sqrt{3}(1-\phi_u)}-2}\right], \quad \text{(C-1)}$$

$$\lambda_r = \frac{\lambda_{\min}}{\lambda_{\max}} = \frac{d_{\text{clay}}}{d_{\text{eff}}}\sqrt{2(1-\phi_u)}, \qquad \text{(C-2)}$$

$$D_p = E - \frac{\ln(\phi_u)}{\ln(\lambda_{\min}/\lambda_{\max})}, \qquad \text{(C-3)}$$

$$A = \frac{\pi d_{\text{eff}}^2}{8}\frac{1}{1-\phi_u}, \qquad \text{(C-4)}$$

where, $\lambda_{\max}$ is maximum pore-diameter, λ_r is pore diameter ratio, D_p is fractal dimension of pores and A is cross-sectional area.

The Euclidean dimension $E = 2$ for a 2D cross section.

Permeability is highly sensitive to changes in grain size (Vadapalli et al., 2014). However, the grain-size information of small reservoir blocks is generally not available. In the absence of measured grain-size information, the following equation can be used to estimate grain diameters of clean sand (d_{sst}) and d_{eff} of shaly sand intervals (Mavko et al., 2009; Vadapalli et al., 2014):

$$d_{\text{sst}} = \sqrt{72K_{\text{av}}}\frac{0.67}{\phi_{u,\text{sst}}}\frac{1 - \phi_{u,\text{sst}}}{\phi_{u,\text{sst}}^{3/2}}, \qquad \text{(C-5)}$$

$$d_{\text{eff}} = \frac{d_{\text{clay}}V_{\text{sh}} + d_{\text{sst}}V_{\text{sst}}}{V_{\text{sh}} + V_{\text{sst}}}. \qquad \text{(C-6)}$$

In equation C-5, the grain size and permeability are interdependent. Thus, we considered the reservoir average permeability (K_{av}) of the clean sand layer as an initial guess to obtain a justifiable sand grain radius. In the absence of data on reservoir permeability, one can estimate K_{av} using a suitable empirical relation, such as the following one derived by Weller et al. (2015a), which we found suitable in the present study, $K_{\text{av}} = 6.77 * 10^{-8}/F^{4.591}$, where F is computed using the well-known formula given by Humble: $F = 0.62/[\phi_{u,\text{sst}}]^{2.15}$.

APPENDIX D

STANDARD ERROR ESTIMATION

The statistical error in MC simulations is often presented in terms of standard deviation (σ), which is the relative deviation of the sample mean from the expectation value. However, most of the time, the expectation value of a physical property is unknown. In this case, the σ is merely an estimate of the relative deviation from the sample mean of N_{run} trials. The sample mean is a random variable as it depends on the success probability of N_{run} trials. If N_{run} is sufficiently large and the samples are uncorrelated, they can fit the desired or actual probability distribution. The sample mean ($\bar{k}$) of N_{run} independent/uncorrelated random simulations is obtained as $\bar{k} = (\sum_{j=1}^{N_{\text{run}}} k_j)/N_{\text{run}}$. If there are corre-

lated samples, the associated additional error measured by τ_{int} needs consideration in estimating standard error (Δ_s). Furthermore, to determine the N_{run} required to overcome initialization bias, obtain a stable mean in equilibrium, and suppress correlation effects through convergence in Δ_s, a faster computation is required. A fast and easy way is to estimate τ_{int} and Δ_s using binning analysis (Janke, 2002, 2008; Ambegaokar and Troyer, 2010). The binning method involves grouping the original simulated series into nonoverlapping bins. Considering the parent series, $k_l^0 \in \{k_1, k_2, \ldots, k_{N_{\text{run}}}\}$, the next level of binned series can be written as $k_l^{B_L} = (k_{2l-1}^{B_L-1} + k_{2l}^{B_L-1})/2$, where $l = 1, 2, 3, \ldots, n_B$. Here, n_B is the number of samples in a binned series given by $n_B = N_{\text{run}}/2^{B_L}$, where binning level $B_L = 1, 2, 3, \ldots, B$ and the maximum binning level is $B = \log_2(N_{\text{run}})$. Thus, starting from the original series (k_l^0), we iteratively create a "binned" series ($k_l^{B_L+1}$) by averaging over two consecutive entries. The mean of the new binned series is the same as the original simulated series. The averaged values are, however, less correlated than the original ones. The τ_{int} at each binning level can be obtained as (Janke, 2002)

$$\tau_{\text{int}} = \frac{S}{2}\left(\frac{\sigma_B^2(k)}{\sigma_P^2(k)}\right), \quad \text{(D-1)}$$

where $S(= N_{\text{run}}/n_B)$ is the bin size. The variance of the parent and binned series are σ_P and σ_B, respectively. The variance of any series can be calculated as $\sigma^2(k) = (\bar{k^2}) - (\bar{k})^2$. The standard error estimate (Δ_s) at each binning level is given as follows:

$$\Delta_s = \sqrt{\frac{\sigma_P^2}{N_{\text{run}}}(1 + 2\tau_{\text{int}})}. \quad \text{(D-2)}$$

In equation D-2, due to correlation effects, Δ_s^2 is increased by a factor of ($2\tau_{\text{int}}$) compared to an uncorrelated case. To analyze convergence in Δ_s, we plot it with respect to n_B.

APPENDIX E

EMPIRICAL RELATIONS

The field-scale implementation of the FARMC method for permeability estimation requires field-scale information about the parameters V_{sh}, ϕ_c, and ϕ_u, which are in general estimated using GR and density logs at site-specific zones in a well. To obtain the field-scale information of these parameters, we used the field-scale ϕ_i in the derived empirical relations. The first empirical relation resulting from the regression analysis between ϕ_i and ϕ_c obtained using density and GR log data in the well P_1 is

$$\phi_c = \phi_i^{\max} - (ae^{-b\phi_i}), \quad \text{(E-1)}$$

where a is a data-dependent constant obtained such that it fits the criteria $\phi_c = 0$ and $\phi_c = \phi_i^{\min}$ for clean sand and shale end members, respectively, as shown in Figure 10a and 10b. Considering the case of clean sand ($\phi_i = \phi_i^{\max}$, $\phi_c = 0$), we obtain $b = [\ln(a) - \ln(\phi_i^{\max})]/\phi_i^{\max}$. The second empirical relation to obtain V_{sh} from ϕ_i is derived using equations B-2 and E-1 and by multiplying with a scaling factor of 1.1 as follows:

$$V_{\text{sh}} = 1.1\frac{\phi_i^{\max} - (ae^{-b\phi_i})}{\phi_i}(1 - \phi_i). \quad \text{(E-2)}$$

The scaling factor is required to increase V_{sh} because the constant b estimated for clean sand leads to underestimation of V_{sh} in shaly sand. The third empirical relation for obtaining ϕ_u from ϕ_i is

$$\phi_u = \phi_i - \phi_c = \phi_i - (\phi_i^{\max} - ae^{-b\phi_i}). \quad \text{(E-3)}$$

The estimates from these empirical relations (equations E-1, E-2, and E-3) are compared with their estimates from GR and density logs in the well P_1 as shown in Figure 10a. It is obvious that ϕ_c, V_{sh}, and ϕ_u are in agreement at higher porosities representing predominantly sand/shaly sand and slightly differ at lower porosities representing predominantly shale, whose $\phi_u \leq \phi_{u,\text{sh}}$ and K are assumed to be zero. Thus, the application of former empirical relations (equations E-1, E-2, and E-3) for predominantly sand and shaly sand zones is admissible.

REFERENCES

Abuseda, H., A. Weller, C.-D. Sattler, and W. Debschutz, 2016, Petrographical and petrophysical investigations of upper Cretaceous sandstones of the South West Sennan field, Western Desert, Egypt: Arabian Journal of Geosciences, 9, 212, doi: 10.1007/s12517-015-2156-1.
Adabala, D., S. P. Ray, and P. K. Gupta, 2007, In-situ combustion technique to enhance heavy oil recovery at Mehsana, ONGC — A success story: Presented at the Middle East Oil and Gas Show and Conference, SPE.
Ambegaokar, V., and M. Troyer, 2010, Estimating errors reliably in Monte Carlo simulations of the Ehrenfest model: American Journal of Physics, 78, 150–157, doi: 10.1119/1.3247985.
Angeleri, G., and R. Carpi, 1982, Porosity prediction from seismic data: Geophysical Prospecting, 30, 580–607, doi: 10.1111/j.1365-2478.1982.tb01328.x.
Ayan, C., H. Hafez, S. Hurst, F. Kuchuk, A. O'Callaghan, J. Peffer, J. Pop, and M. Zeybek, 2001, Characterizing permeability with formation testers: Oilfield Review, 13, 2–23.
Banavar, J. R., and D. L. Johnson, 1987, Characteristic pore sizes and transport in porous media: Physical Review B, 35, 7283, doi: 10.1103/PhysRevB.35.7283.
Bhandari, L., and L. Chowdhary, 1975, Stratigraphic analysis of Kadi and Kalol Formations, Cambay Basin, India: AAPG Bulletin, 59, 856–871, doi: 10.1306/83D91D3A-16C7-11D7-8645000102C1865D.
Binley, A., L. Slater, M. Fukes, and G. Cassiani, 2005, The relationship between frequency dependent electrical conductivity and hydraulic properties of saturated and unsaturated sandstone: Water Resources Research, 41, W12417, doi: 10.1029/2005WR004202.
Bryant, W. R., W. Hottman, and P. Trabant, 1975, Permeability of unconsolidated and consolidated marine sediments, Gulf of Mexico: Marine Georesources & Geotechnology, 1, 1–14, doi: 10.1080/10641197509388149.
Carman, P. C., 1956, Flow of gases through porous media: Academic Press.
Chen, X., G. Yao, J. Cai, Y. Huang, and X. Yuan, 2017, Fractal and multifractal analysis of different hydraulic flow units based on micro-CT images: Journal of Natural Gas Science and Engineering, 48, 145–156, doi: 10.1016/j.jngse.2016.11.048.
Chowdhary, L., 2004, Petroleum geology of the Cambay Basin, Gujarat, India: Indian Petroleum Publishers.
Dimri, V. P., 2000, Application of fractals in earth sciences: CRC Press.
Doyen, P. M., 1988, Porosity from seismic data: A geostatistical approach: Geophysics, 53, 1263–1275, doi: 10.1190/1.1442404.
Feng, Y., B. Yu, K. Feng, P. Xu, and M. Zou, 2008, Thermal conductivity of nanofluids and size distribution of nanoparticles by Monte Carlo simulations: Journal of Nanoparticle Research, 10, 1319–1328, doi: 10.1007/s11051-008-9363-6.
Ge, X., Y. Fan, J. Li, and M. A. Zahid, 2015, Pore structure characterization and classification using multifractal theory — An application in Santanghu Basin of western China: Journal of Petroleum Science and Engineering, 127, 297–304, doi: 10.1016/j.petrol.2015.01.004.
Geng, L., G. Li, M. Wang, Y. Li, S. Tian, W. Pang, and Z. Lyu, 2018, A fractal production prediction model for shale gas reservoirs: Journal of Natural Gas Science and Engineering, 55, 354–367, doi: 10.1016/j.jngse.2018.04.025.

Geng, L., G. Li, P. Zitha, S. Tian, and M. Sheng, 2016, A fractal permeability model for shale gas flow through heterogeneous matrix systems: Journal of Natural Gas Science and Engineering, **35**, 593–604, doi: 10.1016/j.jngse.2016.08.033.

Hampson, D. P., J. S. Schuelke, and J. A. Quirein, 2001, Use of multiattribute transforms to predict log properties from seismic data: Geophysics, **66**, 220–236, doi: 10.1190/1.1444899.

Janke, W., 2002, Statistical analysis of simulations: Data correlations and error estimation, in J. Grotendorst, D. Marx, and A. Muramatsu, eds., Quantum simulations of complex many-body systems: From theory to algorithms: John von Neumann Institute for Computing, 10, 423–445.

Janke, W., 2008, Monte Carlo methods in classical statistical physics, in H. Fehske, R. Schneider, and A. Weiße, eds., Computational many-particle physics: Springer, 79–140.

Jiang, Z., Z. Mao, Y. Shi, and D. Wang, 2018, Multifractal characteristics and classification of tight sandstone reservoirs: A case study from the Triassic Yanchang Formation, Ordos Basin, China: Energies, **11**, 2242, doi: 10.3390/en11092242.

Katz, A., and A. Thompson, 1985, Fractal sandstone pores: Implications for conductivity and pore formation: Physical Review Letters, **54**, 1325, doi: 10.1103/PhysRevLett.54.1325.

Katz, A., and A. Thompson, 1986, Quantitative prediction of permeability in porous rock: Physical Review B, **34**, 8179, doi: 10.1103/PhysRevB.34.8179.

Kozeny, J., 1927, Uber kapillare leitung der wasser in boden: Royal Academy of Science, Vienna, Proceedings, Class I, **136**, 271–306.

Krohn, C. E., 1988, Sandstone fractal and Euclidean pore volume distributions: Journal of Geophysical Research: Solid Earth, **93**, 3286–3296, doi: 10.1029/JB093iB04p03286.

Kuila, U., and M. Prasad, 2013, Specific surface area and pore-size distribution in clays and shales: Geophysical Prospecting, **61**, 341–362, doi: 10.1111/1365-2478.12028.

Kumar, A., N. Bhattacharya, and H. Kharoo, 2008, Time-lapse inversion for monitoring in-situ combustion process in Balol field, India: Proceedings of the 7th International Conference & Exposition on Petroleum Geophysics, SEG, 293.

Kumar, A., N. Bhattacharyya, and S. Mohan, 2006, Cross-equalization for time lapse study in Balol field, India: Proceedings of the 6th International Conference and Exposition on Petroleum Geophysics, 1143–1148.

Kumar, A., and S. Mohan, 2004, Feasibility assessment of a time lapse seismic survey for thermal EOR in Balol field, India, based on rock physics and seismic forward modeling: Proceedings of the 5th International Conference & Exposition on Petroleum Geophysics, SEG, 688–695.

Lai, J., G. Wang, Z. Fan, Z. Zhou, J. Chen, and S. Wang, 2018, Fractal analysis of tight shaly sandstones using nuclear magnetic resonance measurements: AAPG Bulletin, **102**, 175–193, doi: 10.1306/0425171609817007.

Larionov, V., 1969, Radiometry of boreholes: Nedra, 127.

Liu, G., B. Yu, D. Ye, F. Gao, and J. Liu, 2020, Study on evolution of fractal dimension for fractured coal seam under multi-field coupling: Fractals, **28**, 2050072, doi: 10.1142/S0218348X20500723.

Loucks, R. G., 2005, Revisiting the importance of secondary dissolution pores in Tertiary sandstones along the Texas Gulf Coast: Gulf Coast Association of Geological Societies Transactions, **55**, 447–455.

Luffel, D., W. Howard, and E. Hunt, 1991, Travis peak core permeability and porosity relationships at reservoir stress: SPE Formation Evaluation, **6**, 310–318, doi: 10.2118/19008-PA.

Mavko, G., T. Mukerji, and J. Dvorkin, 2009, The rock physics handbook: Tools for seismic analysis in porous media: Cambridge University Press, **1**.

Mavko, G., and A. Nur, 1997, The effect of a percolation threshold in the Kozeny-Carman relation: Geophysics, **62**, 1480–1482, doi: 10.1190/1.1444251.

Neasham, J. W., 1977, The morphology of dispersed clay in sandstone reservoirs and its effect on sandstone shaliness, pore space and fluid flow properties: Annual Fall Technical Conference and Exhibition, SPE.

Nelson, P. H., 1994, Permeability-porosity relationships in sedimentary rocks: The Log Analyst, **35**, 38–62.

Pape, H., C. Clauser, and J. Iffland, 1999, Permeability prediction based on fractal pore space geometry: Geophysics, **64**, 1447–1460, doi: 10.1190/1.1444649.

Pape, H., L. Riepe, and J. R. Schopper, 1987, Theory of self-similar network structures in sedimentary and igneous rocks and their investigation with microscopical and physical methods: Journal of Microscopy, **148**, 121–147, doi: 10.1111/j.1365-2818.1987.tb02861.x.

Pitchumani, R., and B. Ramakrishnan, 1999, A fractal geometry model for evaluating permeabilities of porous preforms used in liquid composite molding: International Journal of Heat and Mass Transfer, **42**, 2219–2232, doi: 10.1016/S0017-9310(98)00261-0.

Radlinski, A., M. Ioannidis, A. Hinde, M. Hainbuchner, M. Baron, H. Rauch, and S. Kline, 2004, Angstrom-to-millimeter characterization of sedimentary rock microstructure: Journal of Colloid and Interface Science, **274**, 607–612, doi: 10.1016/j.jcis.2004.02.035.

Ramakrishnan, B., and R. Pitchumani, 2000, Fractal permeation characteristics of preforms used in liquid composite molding: Polymer Composites, **21**, 281–296, doi: 10.1002/pc.10185.

Robinson, J., L. Slater, A. Weller, K. Keating, T. Robinson, C. Rose, and B. Parker, 2018, On permeability prediction from complex conductivity measurements using polarization magnitude and relaxation time: Water Resources Research, **54**, 3436–3452, doi: 10.1002/2017WR022034.

Ryou, S., 1996, Reservoir permeability distributions from multi-well test sequences in heterogeneous reservoirs: Ph.D. thesis, Texas A&M University.

Sen, P., C. Straley, W. Kenyon, and M. Whittingham, 1990, Surface-to-volume ratio, charge density, nuclear magnetic relaxation, and permeability in clay-bearing sandstones: Geophysics, **55**, 61–69, doi: 10.1190/1.1442772.

Serra, O., 1983, Fundamentals of well-log interpretation: Elsevier.

Sigman, K., 2007, Acceptance-rejection method, lecture notes, https://www.studocu.com/in/document/university-of-calcutta/mathematics-honours/4703-07-notes-arm/11337041, accessed 8 November 2022.

Sokal, A., 1997, Monte Carlo methods in statistical mechanics: Foundations and new algorithms, in C. DeWitt-Morette, P. Cartier, and A. Folacci, eds., Functional integration: Springer, 131–192.

Thomas, E., and H. Ra, 1977, Log derived shale distribution in sandstone and its effect upon porosity, water saturation and permeability: Proceedings of the 6th Formation Evaluation Symposium of the Canadian Well Logging Society in Calgary.

Thomas, E., and U. S. Stieber, 1975, The distribution of shale in sandstones and its effect upon porosity: Presented at the 16th Annual Logging Symposium, SPWLA.

Tiab, D., and E. C. Donaldson, 2015, Petrophysics: Theory and practice of measuring reservoir rock and fluid transport properties: Gulf Professional Publishing.

Vadapalli, U., R. Srivastava, N. Vedanti, and V. Dimri, 2014, Estimation of permeability of a sandstone reservoir by a fractal and Monte Carlo simulation approach: A case study: Nonlinear Processes in Geophysics, **21**, 9–18, doi: 10.5194/npg-21-9-2014.

Vedanti, N., and M. K. Sen, 2009, Seismic inversion tracks in situ combustion: A case study from Balol oil field, India: Geophysics, **74**, no. 4, B103–B112, doi: 10.1190/1.3129262.

Vedanti, N., S. S. Yerramilli, R. C. Yerramilli, M. K. Sen, R. P. Srivastava, and U. Vadapalli, 2015, Integrated reservoir characterization for understanding in situ combustion process in Balol heavy oil field, India: Interpretation, **3**, no. 2, T69–T80, doi: 10.1190/INT-2014-0110.1.

Weller, A., L. Slater, A. Binley, S. Nordsiek, and S. Xu, 2015a, Permeability prediction based on induced polarization: Insights from measurements on sandstone and unconsolidated samples spanning a wide permeability range: Geophysics, **80**, no. 2, D161–D173, doi: 10.1190/geo2014-0368.1.

Weller, A., Z. Zhang, and L. Slater, 2015b, High-salinity polarization of sandstones: Geophysics, **80**, no. 3, D309–D318, doi: 10.1190/geo2014-0483.1.

Weller, A., Z. Zhang, L. Slater, S. Kruschwitz, and M. Halisch, 2016, Induced polarization and pore radius — A discussion: Geophysics, **81**, no. 5, D519–D526, doi: 10.1190/geo2016-0135.1.

Wheatcraft, S. W., and S. W. Tyler, 1988, An explanation of scale-dependent dispersivity in heterogeneous aquifers using concepts of fractal geometry: Water Resources Research, **24**, 566–578, doi: 10.1029/WR024i004p00566.

Xiao, B., J. Fan, and F. Ding, 2012, Prediction of relative permeability of unsaturated porous media based on fractal theory and Monte Carlo simulation: Energy & Fuels, **26**, 6971–6978, doi: 10.1021/ef3013322.

Xu, P., B. Yu, X. Qiao, S. Qiu, and Z. Jiang, 2013, Radial permeability of fractured porous media by Monte Carlo simulations: International Journal of Heat and Mass Transfer, **57**, 369–374, doi: 10.1016/j.ijheatmasstransfer.2012.10.040.

Xue, Y., and P. Bogdan, 2017, Reliable multi-fractal characterization of weighted complex networks: Algorithms and implications: Scientific Reports, **7**, 1–22, doi: 10.1038/s41598-017-07209-5.

Yackinous, W. S., 2015, Understanding complex ecosystem dynamics: A systems and engineering perspective: Academic Press.

Yu, B., 2005, Fractal character for tortuous streamtubes in porous media: Chinese Physics Letters, **22**, 158, doi: 10.1088/0256-307X/22/1/045.

Yu, B., and P. Cheng, 2002, A fractal permeability model for bi-dispersed porous media: International Journal of Heat and Mass Transfer, **45**, 2983–2993, doi: 10.1016/S0017-9310(02)00014-5.

Yu, B., and L. James Lee, 2000, A simplified in-plane permeability model for textile fabrics: Polymer Composites, **21**, 660–685, doi: 10.1002/pc.10221.

Yu, B., and J. Li, 2001, Some fractal characters of porous media: Fractals, **9**, 365–372, doi: 10.1142/S0218348X01000804.

Yu, B., and W. Liu, 2004, Fractal analysis of permeabilities for porous media: AIChE Journal, **50**, 46–57, doi: 10.1002/aic.10004.

Yu, B., M. Zou, and Y. Feng, 2005, Permeability of fractal porous media by Monte Carlo simulations: International Journal of Heat and Mass Transfer, **48**, 2787–2794, doi: 10.1016/j.ijheatmasstransfer.2005.02.008.

Zadeh, H. M., R. P. Srivastava, N. Vedanti, and M. Landrø, 2010, Seismic monitoring of in situ combustion process in a heavy oil field: Journal of Geophysics and Engineering, **7**, 16–29, doi: 10.1088/1742-2132/7/1/002.

Zhang, Z., and A. Weller, 2014, Fractal dimension of pore-space geometry of an Eocene sandstone formation: Geophysics, **79**, no. 6, D377–D387, doi: 10.1190/geo2014-0143.1.

Zou, M., B. Yu, Y. Feng, and P. Xu, 2007, A Monte Carlo method for simulating fractal surfaces: Physica A: Statistical Mechanics and Its Applications, **386**, 176–186, doi: 10.1016/j.physa.2007.07.058.

Biographies and photographs of the authors are not available.